A Novel AHB/LLC Combo Converter Using Numerical Optimal Trajectory Control for Wide Voltage Gain Applications

Yuezhe Wu, Qi Hui, *Student Member, IEEE*, Xiaoyong Ren, *Member, IEEE*, and Zhiliang Zhang, *Senior Member, IEEE*

***Abstract*—The latest universal serial bus (USB) power delivery 3.1 quick charger, requiring 5–48 V output and 240 W maximum output power, demands a wide voltage conversion ratio on the ac–dc converter topology. The traditional solution, either using LLC or asymmetrical half-bridge (AHB) topology, suffers from the compromise of efficiency and voltage gain. This article proposed a novel AHB/LLC combo converter that realizes high efficiency at different output voltage levels. Combined with a novel numerical optimal trajectory control method, the converter could seamlessly switch between two operation modes and thus enjoy the extraordinary dynamic performance. The proposed topology and control method are verified on a 240-W prototype, achieving 97.98% peak efficiency and good dynamic regulation during load transient.**

***Index Terms*—AHB/LLC combo converter, numerical optimal trajectory control (NOTC), USB power delivery (PD), wide voltage gain.**

I. Introduction

THE maturity of wide-bandgap devices, especially gallium nitride (GaN), has greatly propelled the development of quick chargers (QC). A plethora of fast-charging charger products with higher power density, higher efficiency, and greater power have emerged, thanks to the adoption of commercial GaN devices. The latest universal serial bus (USB) power delivery (PD) 3.1 protocol, with an ambition to be applied in most low-power applications, requires QC to provide power outputs ranging from adjustable 5–48 V with a maximum of 5 A/240 W.

The wide output voltage range of QC compatible with the PD3.1 protocol places a high demand on the available conversion ratio of the converter topology to be used. The traditional solutions for QC realization suffer from the tradeoff between high voltage gain and high efficiency. A possible architecture is power factor correction (PFC)+LLC [1], [2]. While an LLC converter can offer high efficiency and compact size, its output voltage range is quite limited. For three-stage solutions like PFC+LLC+Buck or PFC+Buck+LLC found in many off-the-shelf products, the LLC stage generally operates near the resonant frequency, sacrificing the voltage gain for high efficiency [3], [4], [5]. While the Buck converter takes care of adjusting the output, the system efficiency is compromised, especially at low output voltage. By using additional active switches, LLC could switch operations modes between full-bridge and half-bridge (HB) [6], or the secondary rectification circuit could be changed [7], [8]. These methods could extend the voltage conversion range of LLC, but the efficiency is hard to optimize and the dynamic performance is undermined without using dedicated control algorithms [9], [10], [11].

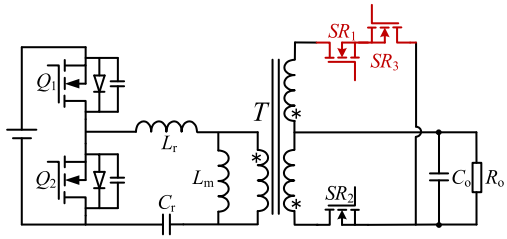

Fig. 1. Topology of AHB/LLC combo converter.

Recently, two-stage flyback-based solutions, including active-clamp flyback (ACF) and asymmetrical HB (AHB) converter, have also gained research interests for QC applications [12], [13]. ACF converter proposed in [14], [15], and [16] effectively recycles the leakage inductance energy and achieves soft switching which enables high efficiency. However, it suffers from relatively high voltage stress. The AHB converter is capable of realizing zero voltage switching (ZVS) [17] and can achieve a wider voltage gain through pulsewidth modulation [18], [19], [20], [21]. However, in terms of full-load efficiency, it is still lower than the LLC solution. Combined with the boost-follower technique on the PFC stage (i.e., variable bus voltage), the low-ac-input efficiency could be greatly improved but it contributes little to the high-ac-input efficiency.

Considering the instinct similarities in LLC and AHB topology, a novel AHB/LLC combo converter shown in Fig. 1 is proposed, leveraging both the advantages of the high efficiency of LLC and the wide output regulation capability of AHB.

Manuscript received 28 March 2024; revised 28 June 2024; accepted 25 July 2024. Date of publication 30 July 2024; date of current version 11 September 2024. This work was supported by the Natural Science Foundation of China under Grant 52177181. Recommended for publication by Associate Editor S. K. Mazumder. *(Corresponding author: Xiaoyong Ren.)*

The authors are with the Aero-Power Sci-Tech Center, Nanjing University of Aeronautics and Astronautics, Nanjing 211116, China (e-mail: wu.yzh@nuaa.edu.cn; hq@nuaa.edu.cn; renxy@nuaa.edu.cn; zlzhang@nuaa.edu.cn).

Color versions of one or more figures in this article are available at https://doi.org/10.1109/TPEL.2024.3435960.

Digital Object Identifier 10.1109/TPEL.2024.3435960

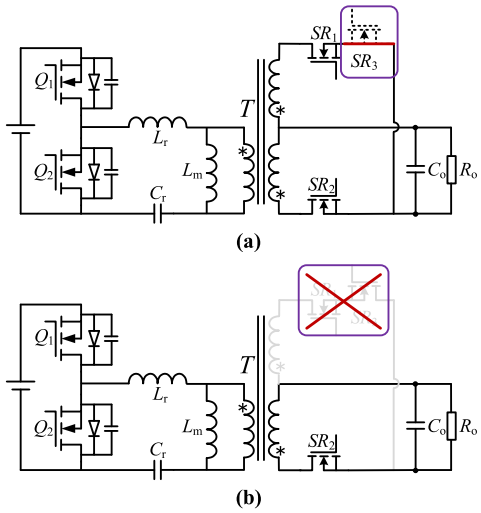

Fig. 2. (a) Topology of LLC mode. (b) Topology of AHB mode.

The converter works in LLC mode at high output voltage and heavy load, whereas switches to AHB mode when low output is requested by the load side. A dedicated numerical optimal trajectory control (NOTC) is also proposed to enhance the dynamic performance of the proposed converter, enabling seamless mode switching during load transient. The rest of this article is organized as follows. Section II elaborates the operation principle of the proposed AHB/LLC combo converter. Section III provides a thorough state-plane analysis of the converter, and an NOTC method is proposed to realize smooth mode transition during load transient. In Section IV, a 5–48 V/5 A PD3.1 QC prototype is fabricated. Efficiency and dynamic performance are evaluated on the prototype to verify the proposed methods. Finally, Section V concludes this article.

II. Principle of AHB/LLC Combo Converter

The proposed AHB/LLC combo converter power circuit is shown in Fig. 1. One of the synchronous rectifiers (SR) in the classical HB LLC converter is replaced with a four-quadrant switch. When SR_3 is turned-ON, the secondary side works in full-wave rectification and the system operates in the LLC mode with the bidirectional magnetization of the magnetizing inductor L_m, as shown in Fig. 2(a). When both SR_1 and SR_3 are turned OFF, the secondary side structure is deformed into half-wave rectification, and the converter operates in the AHB flyback mode with unidirectional magnetization of L_m, as shown in Fig. 2(b).

The relationship between the gain curve of the LLC converter and its design parameters is well established in [15]. It can be observed that the dc gain of the LLC controlled directly by frequency is relatively limited. So, for an LLC converter to meet the USB PD3.1 protocol requirements of a 5–48 V output voltage range, it must operate within an exceptionally wide frequency range.

For the AHB converter, when the primary side switch Q_1 is turned ON, the magnetizing inductor L_m stores energy. When

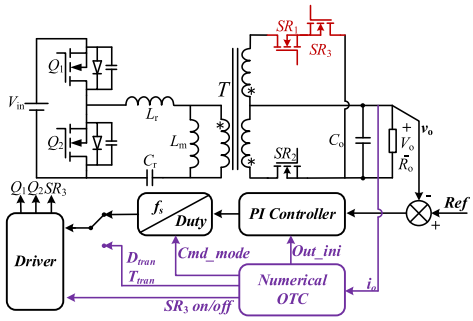

Fig. 3. Block diagram of the proposed NOTC.

Q_2 is conducting, energy is transferred to the secondary side. Similar to the traditional flyback converter, AHB inherently has a flexible gain adjustment capability. Moreover, the addition of the resonant process endows the AHB converter with the ability to achieve ZVS on the primary side and zero current switching (ZCS) on the secondary side. Many publications have conducted detailed analyses of AHB converters, and the voltage gain can be described as [19], [20], [23]

$$V_o = DV_{in}/[n\,(1 + L_r/L_m)]. \tag{1}$$

When L_r is much smaller than L_m, the formula can be expressed as

$$V_o = DV_{in}/n. \tag{2}$$

As a gain of AHB could be readily controlled by duty-cycle modulation, the proposed combo converter will have a wide voltage gain range when working under AHB mode. Also, high efficiency under heavy load and high output is ensured by operating at LLC mode [26]. Therefore, the converter avoids the efficiency issues typically encountered by AHB converters in applications with hundreds of watts while keeping the high-efficiency advantage of the LLC converter.

However, seamless mode switching is a significant challenge for the successful implementation of the proposed converter. Despite the similar structures of AHB and LLC converters, the differences in their operating states necessitate consideration of numerous factors during the switching process. To solve this problem, an NOTC method is proposed to achieve smooth and fast transitions during load transient. Fig. 3 shows the control block diagram, where D_{tran} and T_{tran} represent the special switching duty cycle and period provided by NOTC. The two key control parameters form the special operating pulse width required for a seamless transition. The ON/OFF signal of SR_3 is responsible for changing the converter's topology, and OUT_ini is the initial value of the proportional-integral (PI) controller output after the mode switching is completed. Because the DSP can hardly solve complex high-order differential equations in real time, the basic idea of NOTC is to store the numerical solutions obtained by computer simulation as a look-up table (LUT) in the DSP's random access memory (RAM) or flash memory. Based on the discrete data, the trajectory control is realized.

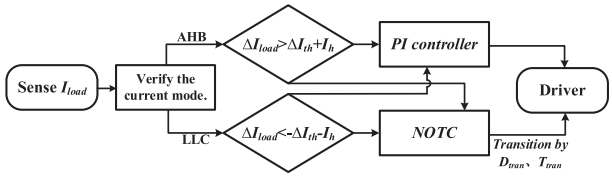

Fig. 4. Control flowchart of the system.

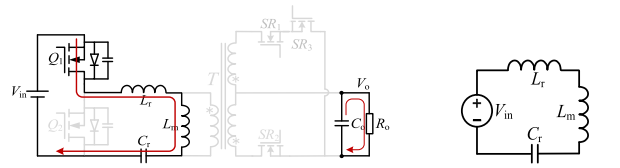

Fig. 5. Equivalent circuit of AHB-I.

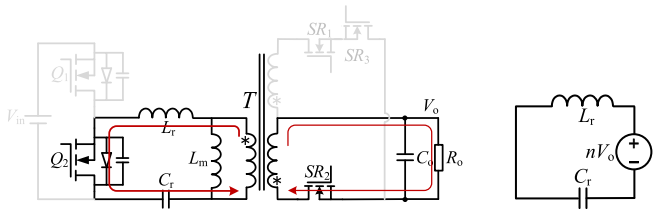

Fig. 6. Equivalent circuit of AHB-II.

The control flowchart of the system is shown in Fig. 4. The converter is controlled by a finite-state machine. $I_{\rm load}$ and $\Delta I_{\rm load}$ represent the load current and the change in load current, respectively. ΔIth is the minimum threshold value of the load current difference between AHB mode and LLC mode. A hysteresis current equal to I_h is set to avoid transition oscillation. The system continuously monitors the load and determines the current mode. When the load change is minor, the PI controller will take care of the perturbation. However, if the load change is significant, the system will initiate a mode transition, and control will be taken over by the NOTC. Based on the data of LUT established in advance, the optimal trajectory of transition is selected. Optimal values of $D_{\rm tran}$ and $T_{\rm tran}$ for seamless transition are provided by the NOTC. The theoretical basis and operation principle of NOTC will be elaborated in the next section.

III. State-Plane Analysis and Trajectory Control in Mode Transition

The state-plane analysis is employed to address the dynamic mode switching problem of the proposed combo converter. By analyzing the steady-state operating trajectories of AHB or LLC before and after the dynamic process, the optimal duty cycle and switching frequency during the transition can be derived. This enables precise control of the operating trajectories to achieve a favorable dynamic response. Through this method, mode transition can be completed in an elegant and rapid way, minimizing oscillation and overshoot.

In general, for resonant converters, different operational states can be characterized by a system of second-order differential equations [17]. By solving these equations, an analytical solution can be obtained. Finally, by normalizing the process with the current factor $V_{\rm in}/Z_0$ and the voltage factor $V_{\rm in}$, a trajectory of normalized i_{LrN} and v_{CrN} can be obtained, where $Z_0 = \sqrt{L_r/C_r}$ is the characteristic impedance.

The operation modes of the AHB/LLC combo converter are complicated and diverse. The following analysis mainly focuses on all key modes exhibited in the proposed combo converter. The key idea to realize seamless mode switching is to find and fully utilize the possible intersection points on state-plane trajectories of both LLC and AHB under different conditions.

A. State-Plane Analysis

1) Analysis of AHB Mode: When $\rm SR_3$ is turned OFF, the AHB/LLC combo converter operates in the AHB mode. The AHB converters are commonly regarded as a type of flyback converter because of its. Moreover, an AHB converter can be also considered as a specific operational state of an LLC resonant converter. Due to the presence of the resonant tank, the state-plane analysis method is appropriate in this case.

The different curves describe the trajectories of the AHB converter in different working conditions, which are composed of three operating modes, namely AHB-I, AHB-II, and AHB-III.

In the mode AHB-I, the primary side main switch Q_1 is ON, and there is no current flowing through the secondary side. The magnetizing inductor $L_{\rm m}$ joins in the resonance, which forms a series resonance with resonant inductor $L_{\rm r}$ and resonant capacitor $C_{\rm r}$. The source voltage across the resonant tank is $V_{\rm in}$. Fig. 5 shows the operational state and the equivalent circuit of AHB-I, from which the trajectory equation of this mode can be derived. The normalized trajectory equation can be given by

$$(v_{CrN}-1)^2+\left(\frac{i_{LrN}}{Z_0/Z_1}\right)^2=(v_{Cr0N}-1)^2+\left(\frac{i_{Lr0N}}{Z_0/Z_1}\right)^2 \tag{3}$$

which is characterized by an ellipse with a center at (1, 0), with the major axis and minor axis determined by I_{Lr0N} and V_{Cr0N}. where $Z_1=\sqrt{(L_m+L_r)/C_r}$ and $Z_0=\sqrt{L_r/C_r}$ are the characteristic impedance.

As shown in Fig. 6, AHB-II occurs when the primary side main switch Q_2 turns ON, and the resonant current flows through the secondary side $\rm SR_2$. In this mode, the magnetizing inductor $L_{\rm m}$ is clamped by the output voltage, where the resonant capacitor $C_{\rm r}$ and the resonant inductor L_r form the series resonant tank. The source voltage across the resonant tank is nV_o. The normalized trajectory equation is given as follows:

$$(v_{CrN}-nV_{oN})^2+i_{LrN}^2=(v_{Cr0N}-nV_{oN})^2+i_{Lr0N}^2 \tag{4}$$

which behaves as a circle. The center located at (nV_{oN}, 0) is determined by the source voltage across the tank, and the radius is $\sqrt{(v_{Cr0N}-nV_{oN})^2+i_{Lr0N}^2}$, which depends on the initial conditions I_{Lr0N} and V_{Cr0N}.

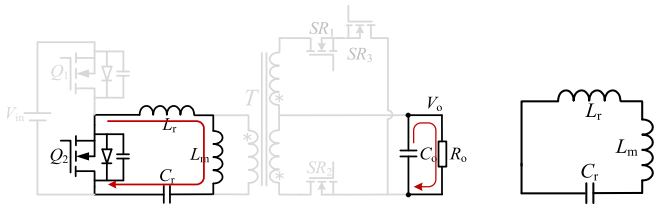

Fig. 7. Equivalent circuit of AHB-III.

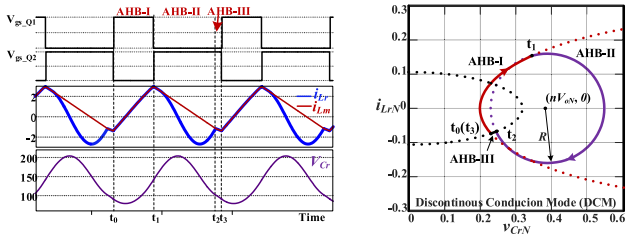

Fig. 8. Time domain waveforms and steady trajectory of AHB in DCM.

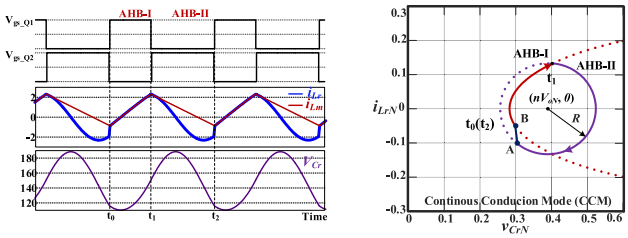

Fig. 9. Time domain waveforms and steady trajectory of AHB in CCM.

During operation mode AHB-III shown in Fig. 7, Q_2 is still ON, but the resonance process formed by L_r and C_r ends when i_{Lr} equals i_{Lm}. There is no current flowing through the secondary side. Similarly to AHB-I, L_m, L_r, and C_r form the series resonant tank. However, the voltage across the resonant tank becomes 0. The normalized trajectory equation is

$$v_{CrN}^2 + \left(\frac{i_{LrN}}{Z_0/Z_1}\right)^2 = v_{Cr0N}^2 + \left(\frac{i_{Lr0N}}{Z_0/Z_1}\right)^2 \tag{5}$$

which is an ellipse with a center (0, 0).

The AHB converter can be classified into three modes, i.e., continuous conduction mode (CCM), critical conduction mode (CRM), and discontinuous conduction mode (DCM), depending on whether the current flowing through the SR_2 naturally goes to zero. Fig. 8 shows the time-domain waveform in DCM and the trajectory locus when mapping the resonant current i_{Lr} and the resonant voltage v_{Cr} to the state plane. In CCM, trajectory consists of three segments, and all modes of AHB are present.

Figs. 9 and 10, respectively, show the CCM and CRM. They are both composed of the AHB-I and AHB-II states. In the CCM, when Q_2 is turned OFF, the ellipse and the circle do not intersect, and the trajectory swiftly connects from point A to point B in a nearly straight line.

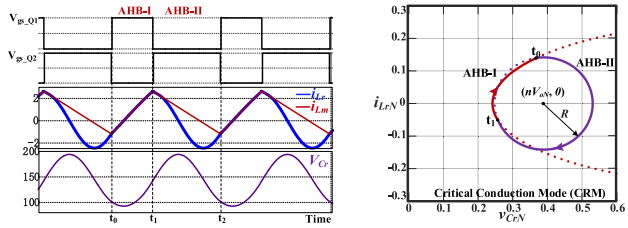

Fig. 10. Time domain waveforms and steady trajectory of AHB in CRM.

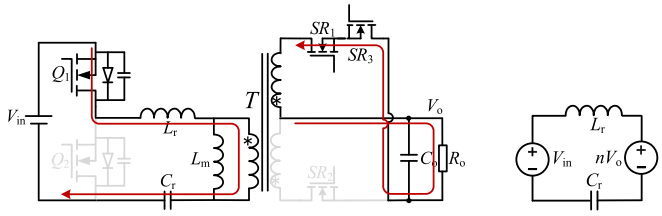

Fig. 11. Equivalent circuit of LLC-I.

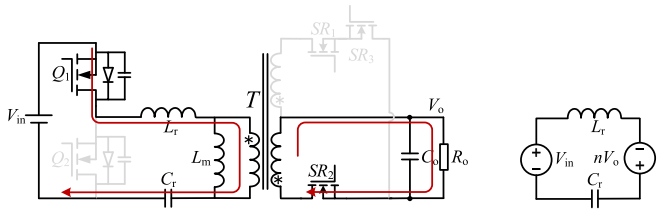

Fig. 12. Equivalent circuit of LLC-II.

2) Analysis of LLC Mode: When SR_3 is turned ON, the AHB/LLC combo converter works as an LLC resonant converter. Under the condition of a 36-V output, the LLC converter operates in the upper resonant state and significantly deviates from the resonance point. Its operational trajectory consists of modes LLC-I, LLC-II, LLC-III, and LLC-IV.

LLC-I occurs when the high-side main switch Q_1 is ON, and the resonant current flows through the secondary side SR_2. In this mode, the magnetizing inductor L_m is clamped by the output voltage. The circuit is in a two-element resonance formed by the resonant inductor L_r and the resonant capacitor C_r. The equivalent circuit is shown in Fig. 11. The source voltage across the resonant tank is V_{in}-nV_o. The normalized trajectory is expressed by

$$\begin{aligned}&[v_{CrN} - (1 - nV_{oN})]^2 + i_{LrN}^2 \\ &\quad = [v_{Cr0N} - (1 - nV_{oN})]^2 + i_{Lr0N}^2\end{aligned} \tag{6}$$

which behaves as a circle with the center (1-nV_{oN}, 0) and the radius is $\sqrt{[v_{Cr0N} - (1 - nV_{oN})]^2 + i_{Lr0N}^2}$.

As shown in Fig. 12, LLC-II occurs when Q_1 is ON, but the current flowing through the secondary side changes its direction and flows through SR_2. This mode is similar to LLC-I, however, the clamping voltage across L_m becomes -nV_o, and the source voltage across the resonant tank changes to V_{in}+nV_o. The

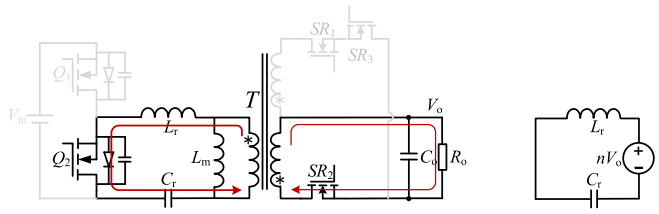

Fig. 13. Equivalent circuit of LLC-III.

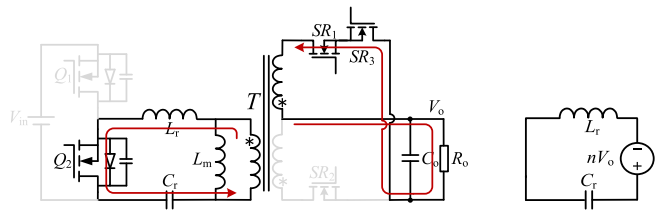

Fig. 14. Equivalent circuit of LLC-IV.

normalized trajectory is expressed as

$$[v_{CrN} - (1 + nV_{oN})]^2 + i_{LrN}^2 = [v_{Cr0N} - (1 + nV_{oN})]^2 + i_{Lr0N}^2 \quad (7)$$

which behaves as a circle with the center $(1+nV_{oN}, 0)$ and the radius is $\sqrt{[v_{Cr0N} - (1 + nV_{oN})]^2 + i_{Lr0N}^2}$.

As shown in Fig. 13 , LLC-III occurs when Q_2 is ON, and the resonant current flows through the secondary side SR_2. In this mode, the converter is also in a two-element resonant operating state. The only difference from LLC-I is the source voltage across the resonant tank becomes nV_o. The normalized trajectory is expressed by

$$(v_{CrN} - nV_{oN})^2 + i_{LrN}^2 = (v_{Cr0N} - nV_{oN})^2 + i_{Lr0N}^2 \quad (8)$$

which behaves as a circle with the center $(nV_{oN}, 0)$ and the radius is $\sqrt{(v_{Cr0N} - nV_{oN})^2 + i_{Lr0N}^2}$.

It is worth noting that the circuit operation principle of this mode is the same as that of the AHB-II. The magnetizing inductor L_m is clamped by the output voltage, and the resonant capacitor C_r and the resonant inductor L_r form the series resonant. Moreover, there is no current flowing through the bidirectional switch branches composed of SR_1 and SR_3. This demonstrates that AHB converters and LLC converters not only share a high degree of similarity in circuit topology but also in operational principles.

LLC-IV occurs when Q_2 is ON, but the current on the secondary side changes its direction, as shown in Fig. 14, flowing through the branch composed of SR_1 and SR_2. Similar to LLC-II, the source voltage across the resonant tank made of L_r and C_r becomes $-nV_o$. The equivalent circuit is shown in Fig. 14. The normalized trajectory is expressed by

$$(v_{CrN} + nV_{oN})^2 + i_{LrN}^2 = (v_{Cr0N} + nV_{oN})^2 + i_{Lr0N}^2 \quad (9)$$

which behaves as a circle with the center $(-nV_{oN}, 0)$ and the radius is $\sqrt{(v_{Cr0N} + nV_{oN})^2 + i_{Lr0N}^2}$.

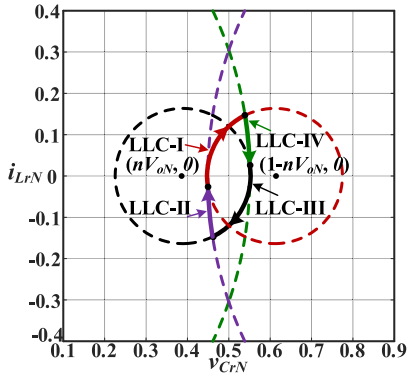

Fig. 15. Steady-state trajectory when $f_s > f_r$.

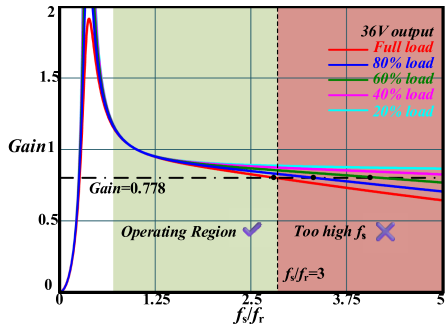

Fig. 16. Voltage gains of LLC in 36-V output.

In Fig. 15, the combo converter operates in LLC mode above ($f_s > f_r$). The trajectory locus is composed of four segments, and the whole is a symmetrical figure.

B. Trajectory Transition From AHB to LLC

The NOTC strategy proposed in this article enables rapid response during load transients, facilitating a smooth transition from AHB mode to LLC mode.

Fig. 16 shows the state-plane trajectory and the time-domain waveforms of the transition process from AHB to LLC. Under the condition of a 36 V output voltage, when facing heavy loads, the converter operates in LLC mode, depicted as the black trajectory. As shown in Fig. 16, for the LLC converter, due to inherent limitations in the ability to adjust the gain, the converter is operating at a high frequency, significantly deviating from the resonance point [27]. As the load decreases, the operating frequency of the converter will further increase, leading to increased losses. Consequently, the performance of the LLC converter will lag that of the AHB converter. Additionally, excessively high operating frequencies pose a significant challenge in terms of performance for the digital controller. Therefore, when the load is lighter, the converter will turn to operate in AHB mode, represented by the orange trajectory. Because the AHB mode is working in CCM mode or close to CRM mode, the trajectory of AHB is approximately composed of two parts, AHB-I and AHB-II. When the load takes a step, the NOTC will take over control at t_0, making the trajectory switch from AHB mode to LLC mode along the blue line.

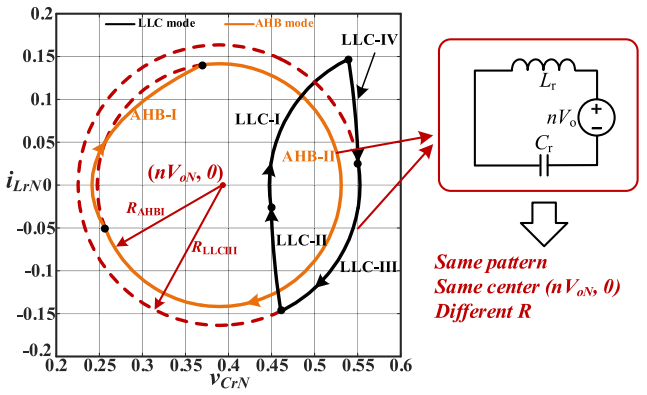

Fig. 17. Similarity between AHB-II and LLC-III.

Based on the analysis above, it can be observed that the operational modes AHB-II and LLC-III of the combo converter exhibit a high degree of similarity, as shown in Fig. 17. The operational states of the switch components and the direction of primary and secondary currents are identical. Specifically, the primary-side main switch Q_2 is ON, and the secondary-side current flows through SR_2. The series resonance tank is formed by L_r and C_r, and the four-quadrant switch formed by SR_1 and SR_3 has no current flowing through. In the state plane, they have the same trajectory pattern and the same center. The only difference is that the radii of the trajectories are inconsistent, due to the different initial values of the states. Therefore, in these two operational modes, it is safe to toggle SR_3 ON and OFF, completely avoiding the potential short-circuit risk caused by the morphing of the secondary-side topology. Exactly, whether switching to AHB mode or LLC mode, it is reliable to toggle SR_3 to change operational state during the resonance period of the two components when Q_2 is ON, that is, during the operation periods of AHB-II and LLC-III.

When the converter needs to switch modes in response to a load step, NOTC takes over control from the PI controller. It will generate two special pulses with precalculated optimal duty cycle and frequency to achieve the switching of the converter's operating mode. As shown in Fig. 18, the transition from AHB to LLC consists of two parts: $t_0{}'$ to $t_2{}'$ (first cycle in AHB mode) and $t_2{}'$ to $t_4{}'$ (second cycle in LLC mode). From the blue line, in the last cycle of AHB mode, the primary side main switch Q_1 maintains the original duty cycle.

$$t_1{}' - t_0{}' = D_{s\_\mathrm{AHB}} \times T_{s\_\mathrm{AHB}}. \tag{10}$$

After the Q_2 turns ON and the secondary-side current flows through SR_2, SR_3 is turned ON during this period. The converter's topology has switched to the LLC resonant converter. Due to the consistency between AHB-II and LLC-III modes, the trajectory will continue to follow the circular equation represented by (4) until reaching $t_2{}'$, where the intersection with LLC-II occurs. The coordinates of $t_2{}'$ can be obtained by solving the

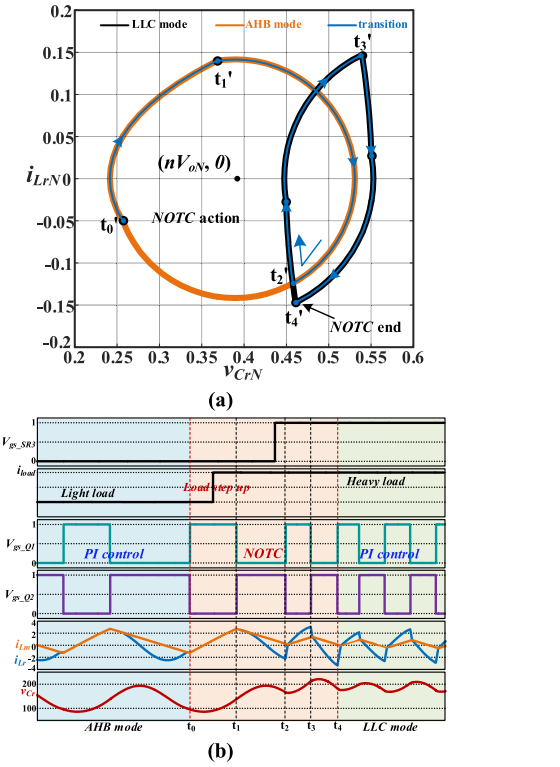

Fig. 18. (a) Trajectory of transition from AHB to LLC. (b) Time-domain waveforms from AHB to LLC.

equations represented by (4) and (7) simultaneously.

$$\begin{cases} (v_{CrN} - nV_{oN})^2 + i_{LrN}^2 = (v_{Cr0N4} - nV_{oN})^2 \\ \qquad\qquad\qquad\qquad +i_{Lr0N4}^2 \\ [v_{CrN} - (1+nV_{oN})]^2 + i_{LrN}^2 = [v_{Cr0N7} - (1+nV_{oN})]^2 \\ \qquad\qquad\qquad\qquad +i_{Lr0N7}^2 \end{cases}. \tag{11}$$

Based on $t_2{}'$, we can determine the ON-time of Q_2 as

$$t_2{}' - t_1{}' = \left[\frac{i_{Lr0N\_t1'}}{v_{Cr0N\_t1'} - nV_{oN}} - \frac{i_{Lr0N\_t2'}}{v_{Cr0N\_t2'} - nV_{oN}}\right] \Big/ \omega_0. \tag{12}$$

Since the resonant inductor L_r and the resonant C_r form a series resonance, $\omega_0 = 1/\sqrt{L_r * C_r}$.

At $t_2{}'$, the primary side switch Q_2 is turned OFF, and the trajectory switches from the AHB-II to LLC-IV, thereby entering the LLC operating mode. During the $t_2{}'$ to $t_4{}'$, as indicated by the state-plane trajectory, it is necessary to appropriately reduce the conduction time of Q_1 to guide the trajectory onto the correct path. The turn-ON time of Q_1 can be obtained by

$$t_3{}' - t_2{}' = \left[\frac{i_{Lr0N\_t3'}}{v_{Cr0N\_t3'} - (1+nV_{oN})} - \frac{i_{Lr0N\_t2'}}{v_{Cr0N\_t2'} - (1+nV_{oN})}\right] \Big/ \omega_1 \tag{13}$$

and OFF-time from t_3' to t_4' is determined by the steady-state switching frequency after the mode transition

$$t_4' - t_3' = 0.5 \times T_{s\_\mathrm{LLC}} \tag{14}$$

where $\omega_1 = 1/\sqrt{(L_m + L_r) * C_r}$ is the parallel resonant frequency for this three-element series-resonant state.

Based on (11)–(14), the period and duty cycle of two key pulses to fulfill the transition could be derived as

$$\begin{aligned} T_{\mathrm{tran\_1st}} = {} & (t_1' - t_0') + (t_2' - t_1') = D_{s\_\mathrm{AHB}} \times T_{s\_\mathrm{AHB}} \\ & + \left[\frac{i_{Lr0N\_t1'}}{v_{Cr0N\_t1'} - nV_{oN}} \right. \\ & \left. - \frac{i_{Lr0N\_t2'}}{v_{Cr0N\_t2'} - nV_{oN}} \right] \Big/ \omega_0 \end{aligned} \tag{15}$$

$$D_{\mathrm{tran\_1st}} = (D_{s\_\mathrm{AHB}} \times T_{s\_\mathrm{AHB}})/T_{\mathrm{tran\_1st}} \tag{16}$$

$$\begin{aligned} T_{\mathrm{tran\_2nd}} = {} & (t_3' - t_2') + (t_4' - t_3') = 0.5 \times T_{s\_\mathrm{LLC}} \\ & + \left[\frac{i_{Lr0N\_t3'}}{v_{Cr0N\_t3'} - (1 + nV_{oN})} \right. \\ & \left. - \frac{i_{Lr0N\_t2'}}{v_{Cr0N\_t2'} - (1 + nV_{oN})} \right] \Big/ \omega_1 \end{aligned} \tag{17}$$

$$D_{\mathrm{tran\_2nd}} = (t_3' - t_2')/T_{\mathrm{tran\_2nd}}. \tag{18}$$

Using the NOTC, the transition from AHB mode to LLC mode under load step conditions is completed. From a viewpoint of state-plane analysis, the proposed NOTC realizes a rapid adjustment of the state trajectory. From a time-domain perspective, this helps the system quickly reach a steady state.

C. Trajectory Transition From LLC to AHB

The trajectory transition from LLC mode to AHB mode is similar to the method introduced in Section III-B.

As shown in Fig. 19(a), the orange line is the trajectory of AHB, the black line is the trajectory of LLC, and the blue ones are transition trajectories. The load decreases from full load to 60% load, and the transition cycle starts at t_0", and the transition cycle ends at t_2". The drives of MOSFETs and key waveforms are shown in Fig. 19(b).

The trajectories of each mode are similar to those in Section III-B, but transition paths are different. Under full load conditions with an output voltage of 36 V, the converter operates in LLC mode. When the load decreases and mode transition is required, the converter will switch to AHB mode within one switching cycle with NOTC. Based on the analysis above, it is important that the toggling of SR_3 occurs during the period when the primary-side switch Q_2 is conducting and the secondary-side current flows through SR_2. This basic principle still needs to be followed during the mode transition of the load-down step. It can be observed that the trajectory equations for AHB-II and LLC-III modes are both circles with the same center (nV_{oN}, 0) but different radii. Therefore, we can extend the operating time of the LLC-III trajectory under LLC mode appropriately to extend it into Region B shown in Fig. 17(a), where Q_2 is turned OFF to complete the transition. The point is marked as point A.

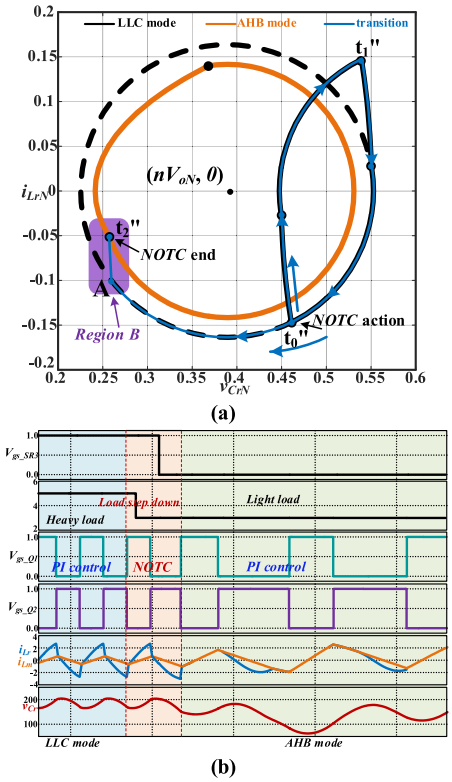

Fig. 19. (a) Trajectory of transition from LLC to AHB. (b) Time-domain waveforms from LLC to AHB.

During this period, SR_3 is turned OFF to switch topology. As the radius of the AHB-I and the switch locus are different, the blue switching trajectory here cannot fully merge with the trajectory of AHB-II. The trajectory between point A and time t_2" can be approximated as a straight line, as they are close in both distance and time. This is reasonable because the phenomenon also occurs in the DCM of the AHB converter. In Region B, the switching trajectory and the AHB-II trajectory represent similar states of the energy storage components in the resonant tank. Switching at this point can minimize oscillation and spikes to a great extent. Additionally, from another standpoint, the AHB converter itself allows operation in DCM mode, which does not lose the soft-switching characteristics of the primary side switches. Therefore, this approach is feasible.

The formula for the duty cycle is derived as follows.

The transition from LLC to AHB consists of one switching cycle (t_0" to t_2"). In this NOTC cycle, the turn-ON time of the primary side switch Q_1 remains the same as the LLC under full load, which is half of the working cycle, from t_0" to t_1".

$$t''_1 - t''_0 = T_{s\_\mathrm{LLC}}/2. \tag{19}$$

Then, it is necessary to determine the switching time t_2" based on point A. We can approximate that the normalized horizontal coordinates of A and t_2'' are the same.

$$\begin{cases} v_{CrN\_t2''} = v_{CrN\_A} \\ i_{LrN\_t2''} = \sqrt{R^2 - (v_{CrN\_A} - nV_{oN})^2} \end{cases}. \tag{20}$$

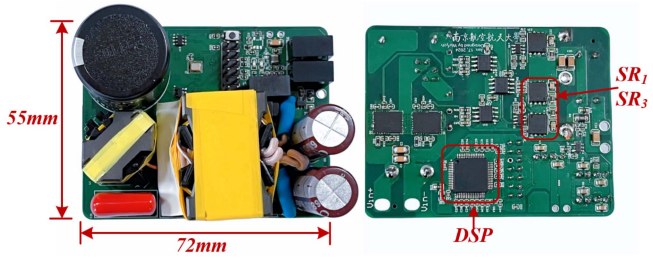

Fig. 20. Hardware prototype.

TABLE I
DESIGN PARAMETERS AND KEY COMPONENT SELECTION

Component Name	Specifications or Values
Magnetizing inductor (L_m)	322.23 μH
Resonant inductor (L_r)	39.78 μH
Transformer turns ratio (n)	4
Resonant capacitator (C_r)	100.26 nF (1000V)
Primary side switch	NV6128/NV6127
Secondary side switch	BSC093N15BS5
Transformer ferrite	PQ 32/25
Inductor ferrite	RM8
DSP	TMS320F280049

Based on equations, we can determine the ON-time of Q_2 as

$$t''_2 - t''_1 = \left[\frac{i_{Lr0N\_t2''}}{v_{Cr0N\_t2''} - nV_{oN}} - \frac{i_{Lr0N\_t1''}}{v_{Cr0N\_t1''} - nV_{oN}}\right] \Big/ \omega_0 \tag{21}$$

where $\omega_0 = 1/\sqrt{L_r * C_r}$ is the series resonant frequency.

Only one pulse is required to complete the mode transition from LLC to AHB. The corresponding period and duty cycle of the pulse can be derived from (19)–(21) as

$$T_{\text{tran}} = (t''_1 - t''_0) + (t''_2 - t''_1) = T_{s\_\text{LLC}}/2 + \left[\frac{i_{Lr0N\_t2''}}{v_{Cr0N\_t2''} - nV_{oN}} - \frac{i_{Lr0N\_t1''}}{v_{Cr0N\_t1''} - nV_{oN}}\right] \Big/ \omega_0 \tag{22}$$

$$D_{\text{tran}} = 0.5 \times T_{s\_\text{LLC}}/T_{\text{tran}}. \tag{23}$$

The NOTC will also provide initial values for the PI controller based on data stored in the DSP. The transition from LLC mode to AHB mode under load step-down conditions is completed. The PI controller takes over the control.

IV. EXPERIMENTAL RESULTS

A 240-W AHB/LLC combo converter prototype with 370 V input and 5–48 V output, fully compatible with the latest PD3.1 protocol requirement, is fabricated to verify the effectiveness of the proposed NOTC, which is shown in Fig. 20. Design parameters and key components selection are given in Table I. The resonant frequency is around 80 kHz. In AHB mode, the converter operates at a fixed frequency of 70 kHz, whereas in LLC mode the switching frequency range is 65–235 kHz.

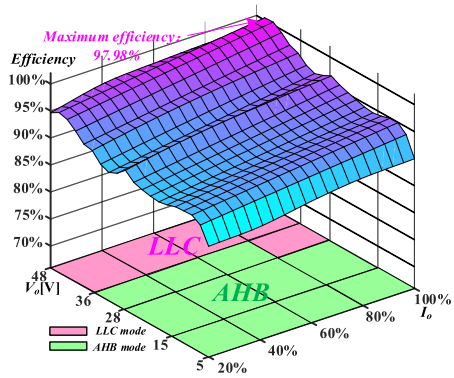

Fig. 21. Efficiency and mode distributions.

To ensure full-load efficiency, the converter should operate near the resonant frequency in LLC mode under full-load conditions, so the turns ratio n is chosen as 4. From the perspective of reducing conduction and switching losses, we prioritize selecting a large L_m. However, we also need to ensure ZVS in both AHB and LLC modes. This implies that L_m cannot be too large either [18], [28] as shown in the following equations:

$$\text{for LLC}, L_m \le \frac{16C_j f_r}{t_{\text{dead}}} \tag{24}$$

$$\text{for AHB}, L_m \le \frac{nV_o(1-D)T_s}{2\left(I_o/n + 2C_j V_{in}/t_{\text{dead}}\right)}. \tag{25}$$

As shown in Fig. 21, based on the PD3.1 specification, the operating modes were classified according to the measured efficiency of the converter, determining the optimal operating range. The maximum output voltage of the converter is 48 V, reaching a power output of 240 W when the output current reaches 5 A. The pink area at the bottom represents the operating range of the LLC mode, and the green area represents the AHB mode. The typical operating waveforms of the main points are illustrated in the Fig. 22.

Under the condition of 48-V output, the waveforms of the output current at 1 and 5 A are shown in Fig. 23(a) and (b). The LLC mode operates in regions below the resonant frequency, achieving primary side ZVS and secondary side ZCS. The converter can achieve a peak efficiency of 97.98%. In the low-voltage output range interval, taking typical output voltages of 5 V and 15 V as examples, traditional HB LLC converters cannot cover this operating range just by changing the operating frequency alone. Thus, the combo converter switches to AHB mode.

Efficiency tests are conducted in accordance with the U.S. DoE6 efficiency regulation. The full-range efficiency of the AHB/LLC combo converter is shown in Fig. 24. The efficiency curves of the converter's full load range under 48 and 36 V output are shown in Fig. 25(a) and (b).

The efficiency of the combo converter proposed in this article is higher than that of others. Compared to the converter built in [25], assuming that PFC efficiency is 98.5% under 230 V ac voltage input, the single-stage efficiency of its dc–dc converter can be estimated. Under the condition of a 48-V output, as

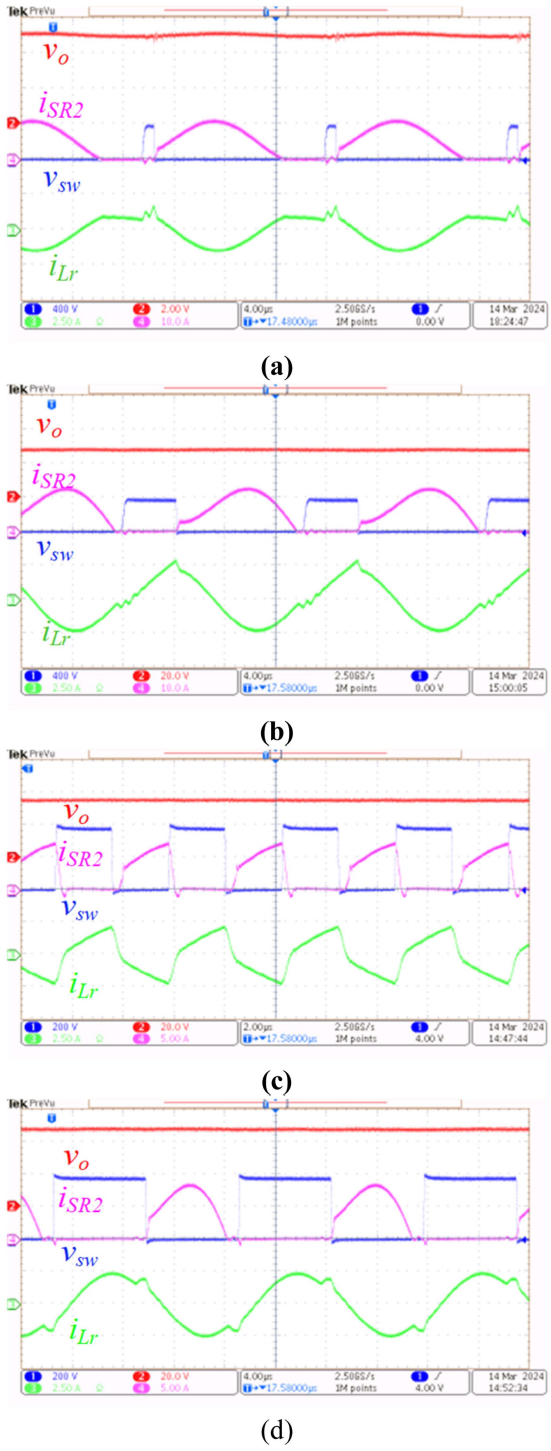

Fig. 22. (a) $V_o = 5$ V and $I_o = 5$ A (AHB). (b) $V_o = 28$ V and $I_o = 5$ A (AHB). (c) $V_o = 36$ V and $I_o = 5$ A (LLC). (d) $V_o = 48$ V and $I_o = 5$ A (LLC).

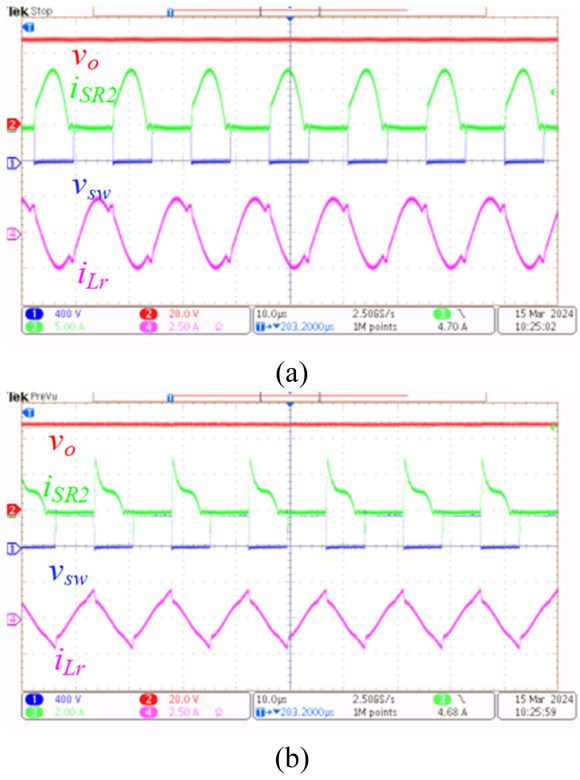

Fig. 23. (a) $V_o = 48$ V and $I_o = 5$ A (LLC). (b) $V_o = 48$ V and $I_o = 1$ A (LLC).

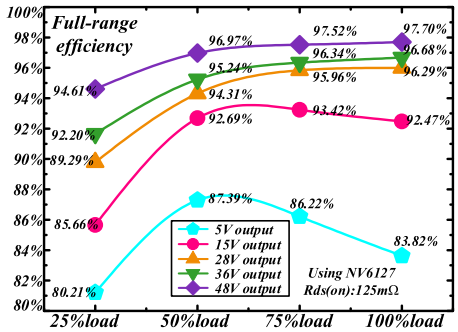

Fig. 24. Full-range efficiency of the combo converter.

shown in Fig. 21, the converter operating in LLC mode shows a significant efficiency advantage compared to existing 240-W AHB solutions. Additionally, at a full load with a 48-V output, it maintains competitive efficiency compared to other LLC converters [29] of the same power level. Under the 36-V condition, as shown in Fig. 21, the converter switches to a different mode depending on the load size. Overall, it still maintains high efficiency.

Under the condition of a 36-V output voltage, the efficiency curves of the different modes are shown in Fig. 26. The black line represents the efficiency of the combo converter in AHB mode, and the red line represents the LLC mode. At full load, the LLC mode maintains its efficiency advantage over the AHB mode, reaching 96.68%. However, as the load decreases and the LLC mode moves away from the optimal operating range, the efficiency of the converter will rapidly decrease, as indicated by the red dashed line. The efficiency of the LLC mode here is lower than that of the AHB mode. To obtain higher efficiency, the combo converter can operate in LLC mode under heavy loads and switch to AHB mode under light loads. Thus, when

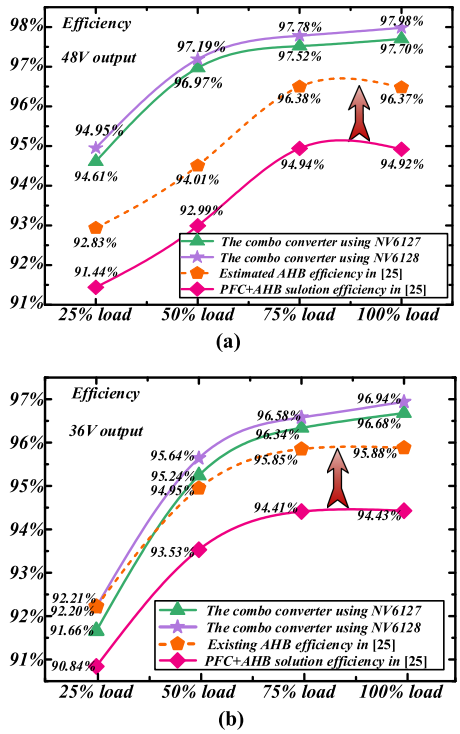

Fig. 25. (a) Efficiency curves under 48-V output. (b) Efficiency curves under 36-V output.

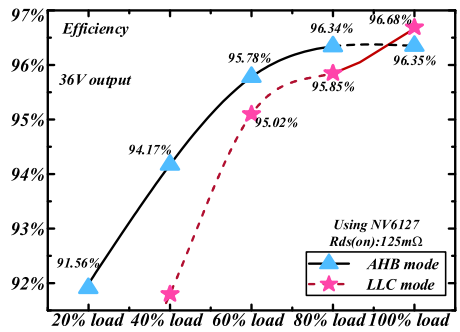

Fig. 26. Efficiency curves of different modes under 36-V output.

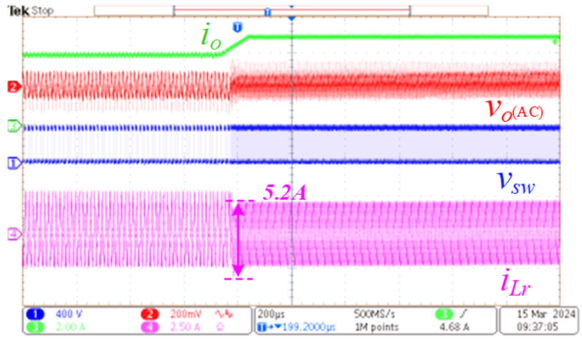

Fig. 27. Response from AHB to LLC (from 4 to 5 A) with NOTC.

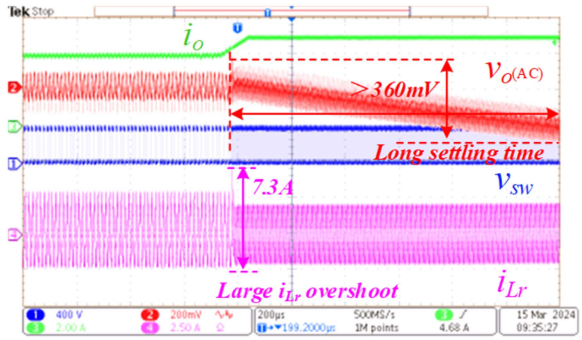

Fig. 28. Response from AHB to LLC (from 4 to 5 A) with PI controller.

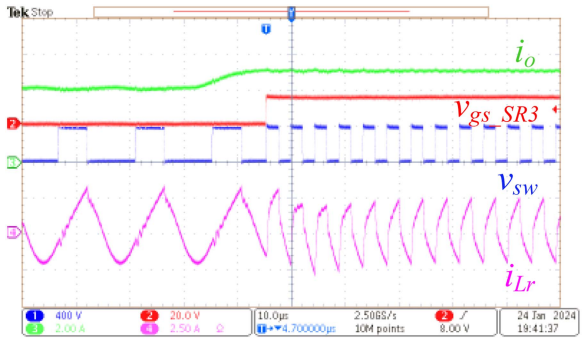

Fig. 29. NOTC at the transition moment (from AHB to LLC).

the load changes and a mode transition is required, the converter will respond quickly using the proposed NOTC based on the optimal operating range.

Fig. 27 shows the waveform of mode-switching from AHB to LLC with NOTC when the load steps from 4 to 5 A. The state variables follow the optimal trajectory, achieving rapid mode switching and excellent dynamic response. As a comparison, another switching experiment controlled by a PI controller is shown in Fig. 28. When using a PI controller, at the same time scale, the system does not reach a steady state. The settling time and the undershoot of the output voltage are significantly increased. This demonstrates the effectiveness of the proposed NOTC control strategy.

In Fig. 29, the mode transition process is shown as zoomed-in, illustrating the conduction timing of SR_3. After the load change, NOTC responds rapidly. The resonant current i_{Lr} is adjusted to a state close to the LLC steady-state with the minimum time, effectively reducing oscillations and overshoot.

The dynamic response of load step-down from 5 to 3 A with the proposed NOTC is shown in Fig. 30. As a comparison, Fig. 31 shows the transition process using the same PI controller. The NOTC significantly improves the dynamic performance of the mode transition from LLC to AHB. The undershoot can be suppressed well and the setting time is reduced as well. It can be also observed that under NOTC, the overshoot and oscillations of i_{Lr} are well constrained within a reasonable range.

Finally, the zoom-in waveform at the transition from LLC to AHB is shown in Fig. 32. With the assistance of NOTC, the

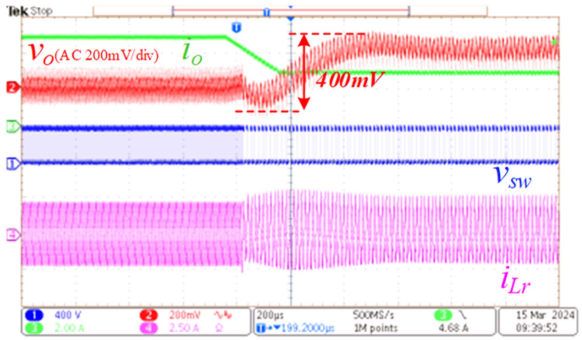

Fig. 30. Response from LLC to AHB (from 5 to 3 A) with NOTC.

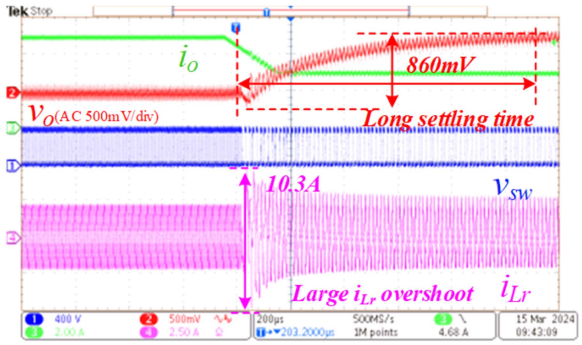

Fig. 31. Response from LLC to AHB (from 5 to 3 A) with PI controller.

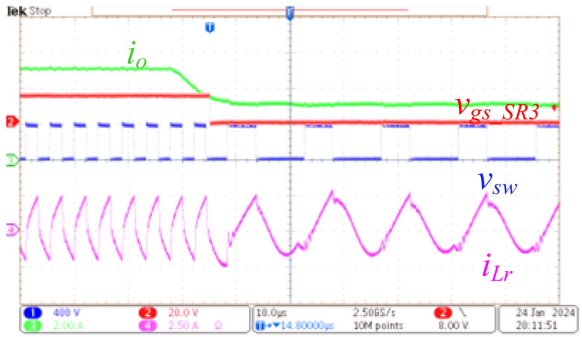

Fig. 32. NOTC at the transition moment (from LLC to AHB).

resonant current i_{Lr} can be settled to the light-load AHB mode in the minimum time.

V. Conclusion

A novel AHB/LLC combo converter enhanced by a dedicated NOTC algorithm is proposed for the PD3.1 QC application, enabling ultrawide voltage gain capability. Operation principles of the proposed converter are provided along with a thorough state-plane analysis, which forms the theoretical basis of the proposed NOTC method. A 240-W PD3.1 QC prototype is fabricated and an excellent peak efficiency of 97.78% is achieved. Very smooth mode switching based on the NOTC is also realized, with very low output variation observed during load transient.

References

[1] B. Kim, K. Park, C. Kim, B. Lee, and G. Moon, "LLC resonant converter with adaptive link-voltage variation for a high-power-density adapter," *IEEE Trans. Power Electron.*, vol. 25, no. 9, pp. 2248–2252, Sep. 2010.

[2] C. Bhuvaneswari and R. S. R. Babu, "A review on LLC resonant converter," in *Proc. Int. Conf. Comput. Power Energy Inf. Commun.*, 2016, pp. 620–623.

[3] B. Lu, W. Liu, Y. Liang, F. C. Lee, and J. D. van Wyk, "Optimal design methodology for LLC resonant converter," in *Proc. 21st Annu. IEEE Appl. Power Electron. Conf. Expo.*, 2006, pp. 533–538.

[4] M. Su, Q. Ouyang, G. Deng, G. Xu, Y. Sun, and W. Xiong, "Modified topology and PWM modulation for bidirectional LLC-DCX converter with center-tapped transformer," *IEEE Trans. Transport. Electrific.*, vol. 8, no. 3, pp. 3907–3920, Sep. 2022.

[5] W. Hao, J. Gong, X. Zhao, C. Yeh, and J. Lai, "Analysis of diode reverse recovery effect on ZVS condition for GaN-based LLC resonant converter," *IEEE Trans. Power Electron.*, vol. 34, no. 12, pp. 11952–11963, Dec. 2019.

[6] Z. Liang, R. Guo, G. Wang, and A. Huang, "A new wide input range high efficiency photovoltaic inverter," in *Proc. IEEE Energy Convers. Congr. Expo.*, 2010, pp. 2937–2943.

[7] M. Shang and H. Wang, "A LLC type resonant converter based on PWM voltage quadrupler rectifier with wide output voltage," in *Proc. IEEE Appl.Power Electron. Conf. Expo.*, 2017, pp. 1720–1726.

[8] H. Wang and Z. Li, "A PWM LLC type resonant converter adapted to wide output range in PEV charging applications," *IEEE Trans. Power Electron.*, vol. 33, no. 5, pp. 3791–3801, May 2018.

[9] M. M. Jovanović and B. T. Irving, "On-the-fly topology-morphing control—Efficiency optimization method for *LLC* resonant converters operating in wide input- and/or output-voltage range," *IEEE Trans. Power Electron.*, vol. 31, no. 3, pp. 2596–2608, Mar. 2016.

[10] D. Sha and X. Yang, "Wide voltage input full bridge(FB)/half bridge(HB) morphing-based *LLC* dc–dc converter using numerical optimal trajectory control," *IEEE Trans. Ind. Electron.*, vol. 70, no. 4, pp. 3697–3707, Apr. 2023.

[11] J. Chen, J. Xu, and Y. Wang, "Seamless control of full-bridge and half-bridge topology morphing *LLC* converter based on state plane analysis," *IEEE Trans. Power Electron.*, vol. 39, no. 1, pp. 198–211, Jan. 2024.

[12] X. Huang, Y. Lei, Y. Zhou, W. Du, and J. Zhang, "An ultra-high efficiency high power density 140W PD3.1 ac-dc adapter using GaN power ICs," in *Proc. IEEE Appl. Power Electron.Conf. Expo.*, 2023, pp. 1252–1258.

[13] X. Huang, J. Feng, W. Du, F. C. Lee, and Q. Li, "Design consideration of MHz active clamp flyback converter with GaN devices for low power adapter application," in *Proc. IEEE Appl. Power Electron. Conf. Expo.*, 2016, pp. 2334–2341.

[14] Y. Yan, T. Wang, Y. Wang, M. Zhu, H. Tang, and Q. Qian, "Adaptive dead-time and partial-ZVS regulation for GaN-based active clamp flyback converter with predictive hysteresis current mode control," *IEEE Trans. Power Electron.*, vol. 38, no. 9, pp. 10782–10797, Sep. 2023.

[15] C. E. Kim, J. Baek, and J.-B. Lee, "Improved three switch-active clamp forward converter with low switching and conduction losses," *IEEE Trans. Power Electron.*, vol. 34, no. 6, pp. 5209–5216, Jun. 2019.

[16] C. -C. Kuo et al., "A dynamic resonant period control technique for fast and zero voltage switching in GaN-based active clamp flyback converters," *IEEE Trans. Power Electron.*, vol. 36, no. 3, pp. 3323–3334, Mar. 2021.

[17] L.M. Wu and C.Y. Pong, "A half bridge flyback converter with ZVS and ZCS operations," in *Proc. 7th Int. Conf. Power Electron.*, Oct. 2007, pp. 876–882.

[18] M. Li, Z. Ouyang, and M. A. E. Andersen, "Analysis and optimal design of high-frequency and high-efficiency asymmetrical half-bridge flyback converters," *IEEE Trans. Ind. Electron*, vol. 67, no. 10, pp. 8312–8321, Oct. 2020.

[19] M. Li, Z. Ouyang, and M. A. E. Andersen, "A high efficiency and high power density asymmetrical half-bridge flyback converter for data centers," in *Proc. 47th Annu. Conf. IEEE Ind. Electron. Soc.*, 2021, pp. 1–6.

[20] Y.-F. Chen, T. D. Nguyen, J.-Y. Lin, Y.-C. Hsieh, and H.-J. Chiu, "Hybrid-switching asymmetrical half-bridge flyback dc-dc converter," in *Proc. IEEE Int. Conf. Ind. Technol.*, 2016, pp. 1313–1317,.

[21] A. Medina-Garcia, F. J. Romero, D. P. Morales, and N. Rodriguez, "Advanced control methods for asymmetrical half-bridge flyback," *IEEE Trans. Power Electron.*, vol. 36, no. 11, pp. 13139–13148, Nov. 2021.

[22] G. Ivensky, S. Bronshtein, and A. Abramovitz, "Approximate analysis of resonant LLC dc-dc converter," *IEEE Trans. Power Electron.*, vol. 26, no. 11, pp. 3274–3284, Nov. 2011.

[23] L. Huber and M. M. Jovanović, "Analysis, design, and performance evaluation of asymmetrical half-bridge flyback converter for universal-line-voltage-range applications," in *Proc. IEEE Appl. Power Electron. Conf. Expo.*, 2017, pp. 2481–2487.
[24] W. Feng, F. C. Lee, and P. Mattavelli, "Simplified optimal trajectory control (SOTC) for LLC resonant converters," *IEEE Trans. Power Electron.*, vol. 28, no. 5, pp. 2415–2426, May 2013.
[25] Infineon Technologies, "240 W USB-PD evaluation board with PFC + hybrid flyback combo IC XDP^{TM} XDPS2222," Infineon Technol., Neubiberg, Germany, Eng. Ref. ER_2305_PL21_2307_083641, Sep. 2023. [Online]. Available: https://www.infineon.com
[26] H. Wen, Y. Liu, D. Jiao, C.-S. Yeh, and J.-S. Lai, "Design principles and optimization considerations of a high frequency transformer in GaN based 1 MHz 2.8 kW LLC resonant converter with over 99% efficiency," in *Proc. IEEE Appl. Power Electron. Conf. Expo.*, 2021, pp. 1939–1944.
[27] Z. Yang, J. Wang, H. Ma, and J. Du, "A wide output voltage LLC series resonant converter with hybrid mode control method," in *Proc. IEEE 2nd Int. Future Energy Electron. Conf.*, 2015, pp. 1–5.
[28] U. Kundu, K. Yenduri, and P. Sensarma, "Accurate ZVS analysis for magnetic design and efficiency improvement of full-bridge LLC resonant converter," *IEEE Trans. Power Electron.*, vol. 32, no. 3, pp. 1703–1706, Mar. 2017.
[29] Application Engineering Department, "240 W LLC CV/CC power supply using HiperLCS^{TM} LCS708HG and LinkSwitch^{TM}-TNLNK302D," Power Integr., San Jose, CA USA, Rep. DER-850, Jan. 2020. [Online]. Available: https://www.power.com

Yuezhe Wu was born in Henan, China, in 2000. He received the B.S. degree in electrical engineering in 2022 from Nanjing University of Aeronautics and Astronautics, Nanjing, China, where he is currently working toward the M.S. degree in electrical engineering.

His research interests include wide-bandgap device applications and electromagnetic interference modeling.

Qi Hui (Student Member, IEEE) received the B.S. and M.S. degrees in electrical engineering in 2016 and 2019, respectively, from Nanjing University of Aeronautics and Astronautics, Nanjing, China, where he is currently working toward the Ph.D. degree in electrical engineering.

From 2019 to 2022, he was a Staff Applications Engineer with Navitas Semiconductor Inc. His research interests include high-bandwidth current measurement and electromagnetic interference modeling.

Mr. Hui won the Grand Prize in the IEEE International Future Energy Challenge 2016. He was the recipient of the Best Presentation Award at the IEEE Applied Power Electronics Conference and Exposition 2019.

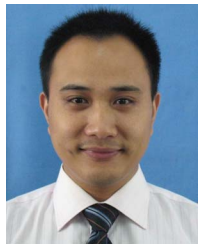

Xiaoyong Ren (Member, IEEE) received the B.S., M.S., and Ph.D. degrees in electrical engineering from Nanjing University of Aeronautics and Astronautics, Nanjing, China, in 2002, 2005, and 2008, respectively.

From 2009 to 2011, he was a postdoctoral researcher with the Center for Power Electronics Systems, Virginia Polytechnic Institute and State University, Blacksburg, VA, USA. He is currently a Professor with the Department of Electrical Engineering, Nanjing University of Aeronautics and Astronautics. His research interests include converter control techniques, wide-bandgap device applications, wireless power transmission, and renewable power systems.

Dr. Ren was among the top three finalists in the Siligery Power Electronics Design Competition in 2015. He led the student teams to win the Grand Prize Award in the International Future Energy Challenge in 2016.

Zhiliang Zhang (Senior Member, IEEE) received the B.S. and M.S. degrees in electrical engineering from Nanjing University of Aeronautics and Astronautics, Nanjing, China, in 2002 and 2005, respectively, and the Ph.D. degree in electrical engineering from the Department of Electrical and Computer Engineering, Queen's University, Kingston, ON, Canada, in 2009.

He is currently a Professor with the Aero-Power Sci-Tech Center, Nanjing University of Aeronautics and Astronautics. He authored or coauthored 40 papers in IEEE TRANSACTIONS ON POWER ELECTRONICS. His current research focuses on high-frequency power conversion with wide-bandgap devices.

Dr. Zhang has been an Associate Editor for the IEEE JOURNAL OF EMERGING AND SELECTED TOPICS OF POWER ELECTRONICS, since July 2018.